

**Ultrafast spin transfer and spin logic gates in linear Ni substituted polyacene structures**

Xiufang Liang <sup>1,2</sup>, Shangjie Ma,<sup>1</sup> Bo Ma,<sup>1</sup> Yiming Zhang <sup>3</sup>, Jing Liu,<sup>4</sup> Chun Li <sup>5,6</sup>, Georgios Lefkidis,<sup>7,5</sup> Wolfgang Hübner,<sup>7</sup> and Wei Jin <sup>1,\*</sup>

<sup>1</sup>*School of Physics and Information Technology, Shaanxi Normal University, Xi'an 710119, China*

<sup>2</sup>*School of Materials Science and Engineering, Sun Yat-sen University, Guangzhou 510275, China*

<sup>3</sup>*School of Science, Xi'an University of Architecture and Technology, Xi'an 710055, China*

<sup>4</sup>*Institute of Theoretical Chemistry, Ulm University, 89081 Ulm, Germany*

<sup>5</sup>*School of Mechanics, Civil Engineering and Architecture, Northwestern Polytechnical University, Xi'an 710072, China*

<sup>6</sup>*Research and Development Institute of Northwestern Polytechnical University in Shenzhen, Shenzhen 518057, China*

<sup>7</sup>*Department of Physics, RPTU Kaiserslautern-Landau, P.O. Box 3049, 67653 Kaiserslautern, Germany*



(Received 3 December 2023; accepted 1 February 2024; published 22 February 2024)

By using the high-level quantum chemistry method, we investigate the electronic and magnetic properties of Ni substituted polyacene structures as well as the laser-induced ultrafast spin dynamics and related spin logic gates. It is found that among the 61 lowest many-body states for each structure, the states with spin localized on a single magnetic atom mainly concentrate in the lower-energy region, while the states with spin localized on fused benzene rings are located in the higher-energy region. As the acene length becomes longer, the amount of states with spin localization on Ni atoms increases and the possibility of finding states with spin localization on benzene rings gets larger. Through the exploration of laser-induced spin dynamics in these structures, we find that different structures achieve different types of spin-transfer scenarios. Especially, although there exist several states with spin localization on different magnetic atoms for all the structures, the transfer between the two Ni atoms via one  $\Lambda$  process is only achieved in  $\text{Ni}_2(\text{C}_{18}\text{H}_{10})$ ,  $\text{Ni}_2(\text{C}_{22}\text{H}_{12})$ , and  $\text{Ni}_2(\text{C}_{38}\text{H}_{20})$ . However, the indirect transfer between two Ni atoms is possible through several bridging  $\Lambda$  processes. Based on the achieved spin scenarios and by appropriately defining the bit information according to the spin localization and directions of the initial and final states, two types of ultrafast spin logic gates, i.e., SWAP and XOR, are constructed. The results obtained in these carbon-based magnetic structures provide valuable insights into their electronic structures and ultrafast spin manipulation and show their potential applications in future molecular spintronic devices and quantum computing.

DOI: [10.1103/PhysRevB.109.064419](https://doi.org/10.1103/PhysRevB.109.064419)

## I. INTRODUCTION

Recently, exploiting the spin degree of freedom as an information carrier in addition to the electronic charge to store and process information becomes increasingly appealing in today's (nano)spintronics technology. The related spintronic devices possess the properties of high density, low power consumption, and nonvolatility, and thus hold much promise in logic functionality and device applications [1,2]. Meanwhile, inspired by the laser pulse induced ultrafast demagnetization phenomenon observed in 1996 [3], optically driven spin dynamics has received extensive attention due to its great potential in the ultrafast information processing and logic computing [4–10]. Therefore, towards the goal of developing another generation of spintronic devices with advancing fast response and extraordinarily large capacity and wider applications in quantum information and computing, seeking suitable magnetic molecular materials with attractive properties and functionalities for realizing specific ultrafast spin dynamics whose efficiency and performance can be engineered by ex-

ternal stimuli (such as laser pulses) becomes one of the most intriguing and blossoming scientific issues.

Among various fascinating candidate systems towards molecular spintronics, polycyclic aromatic hydrocarbons consisting of linearly fused benzene rings, the so-called  $n$ -acenes species ( $\text{C}_{4n+2}\text{H}_{2n+4}$ ), hold much promise owing to their unique structural geometries and electronic features [11–17]. Polyacenes are halfway between 2D graphene nanoflakes [18] and 1D polyacetylene chains [19], and therefore exhibit advantages from both worlds. They are relatively easy to manufacture and they have a flat geometry (unlike polyacetylene chains, which can be easily bent and twisted, and thus their long-range conjugation can be disrupted [20,21]). Furthermore, one can synthesize long nanoribbons [22,23], even with bifurcations [24], and thus they can conceptually be used as a basis for complex stable integrated nanospintronic devices. Different  $n$ -acene series, such as naphthalene ( $\text{C}_{18}\text{H}_{12}$ ), pentacene ( $\text{C}_{22}\text{H}_{14}$ ), hexacene ( $\text{C}_{26}\text{H}_{16}$ ), heptacene ( $\text{C}_{30}\text{H}_{18}$ ), octacene ( $\text{C}_{34}\text{H}_{20}$ ), nonacene ( $\text{C}_{38}\text{H}_{22}$ ), and decacene ( $\text{C}_{42}\text{H}_{24}$ ), have attained tremendous experimental and theoretical consideration with respect to their synthesis, stability, and spectroscopic, electronic, and magnetic properties [25–33]. Several conjugated  $\pi$ -electron system-based field-

\*jinwei@snnu.edu.cn

effect transistors and organic photovoltaic cells have also been proposed and constructed [34,35] by utilizing their high field effect, long exciton diffusion length, and well tunable photo-physical properties.

As for the magnetic property, the diversity of magnetism in these structures and the length effect have been investigated. For instance, the shorter acene (with  $n$  less than six) have been shown to hold a singlet state [36,37]. A magnetic ground-state configuration for longer acene molecules (with  $n$  more than seven) has been attained by Jiang and Dai [38]. The findings that larger oligoacenes possess an open-shell singlet ground state (i.e., antiferromagnetic) has also been proposed in Refs. [38,39]). Recently, a nonmagnetic-antiferromagnetic (NM-AFM) ground-state transition in polyacenes was found at a critical length of  $n=7$  rings and the mechanism of this length-induced magnetism was also analyzed [40]. To further tune their magnetic properties for prominent and designated performance and to enrich the applications broadness, the research into hybrids of magnetic metal species and these  $\pi$ -functional materials, known as magnetically functionalized carbon-based nanostructures, has become an intriguing topic for next-generation spintronic devices. For example, Muz *et al.* investigated the structural and optoelectronic properties of  $3d$ -transition metal (Cu, Fe, Mn, Ni, V, and Zn)-doped pentacene  $\pi$ -conjugated organic molecules [41] by using the density functional theory (DFT), and found that the HOMO-LUMO band gap (i.e., the gap between the highest occupied molecular orbital HOMO and the lowest unoccupied molecular orbital LUMO) of V-doped compounds considerably decreases (which thus is more conductive) compared to that of pentacene, while the Ni-doped pentacene possesses a higher band gap and thus higher chemical reactivity. Using the nonequilibrium Green's function formalism in conjunction with DFT method, the spin-dependent transport on Ni-( $n$ -acene)-Ni ( $n = 1 \sim 15$ ) junctions has been explored [42]. The results showed that the induced magnetic moments of small acene molecules were higher than those of longer acenes, and concluded that the spin-dependent electron transport can be engineered by an appropriate choice of the metallic electrodes and the change of the size of  $n$ -acene molecules. In addition, through the investigation of the electronic structure and transport properties by using the similar method, the system Au/ $n$ -acene/Au was found to be capable of acting as an efficient spin filter with potential application in organic spintronics [43].

All the above works made great contributions to a systematic and comprehensive understanding of the properties of  $n$ -acenes species and show their tremendous potential applications in high-performance molecular magneto-electronics or spintronics. However, the ultrafast spin manipulation, which is significant for the design of nanospintronic devices and future high-speed spin logic gates and microchips, is still largely unexplored. Previously, we have investigated the ultrafast laser-induced spin transfer on a zigzag carbon chain with Ni atoms attached at each end, and found the conjugated C-C bonds allow for spin transfer at a distance comparable to the CMOS (i.e., complementary metal oxide semiconductor) scale [44]. In the present paper, we continue our systematic study of carbon-based structures which can physically interconnect active magnetic-logic centers [44–47], inves-

tigating the electronic structures, magnetic properties, and laser-induced ultrafast spin dynamics as well as logic functionality in molecular systems Ni-( $C_{4n+2}H_{2n+2}$ )-Ni ( $n=4-9$ ). Here, different from the case in which the two  $3d$  transition metals (TM) are separately doped on the meso-point of the pentacene [41], the configuration with two distal H atoms of the linearly fused benzene rings substituted by two Ni atoms is considered. Such structural constituent acts much closer to practical device since the linearly fused benzene rings can serve as spin or charge transmission vessel in carbon-based spintronics and circuits.

The rest of this paper is organized as follows: the theoretical method of our research is introduced in Sec. II. Section III presents the geometric configurations and features of the complexes, followed by the analysis of the electronic structures and spin localization in Sec. IV. Then, the results of several spin-transfer scenarios achieved in specific structures are demonstrated and analyzed in Sec. V, based on which in Sec. VI the spin logic gates are constructed. The summary of our work is given in Sec. VII.

## II. THEORETICAL METHODS

By using the GAUSSIAN 16 package [48], we perform the Hartree-Fock (HF) calculation for geometric optimization and the subsequent infrared spectra calculation for the confirmation of their stability. To keep the balance between calculation cost and accuracy for such strongly correlated systems, the Los Alamos basis set with scalar relativistic effective core potential (e.g., Ni [8s5p5d/3s3p2d]) for the Ni atoms and STO-3G for the C and H atoms are chosen [49]. To provide a more accurate, high-level description of the electronic structures, the symmetry-adapted cluster configuration interaction method (SAC-CI) is adopted [50]. In this method, the wave functions take the multideterminantal form and include various virtual excitations which enable to take both the static and dynamical correlations into account on an equal footing. Here, the former correlation is related to magnetization and the latter is responsible for charge transfer and optical activity, and thus is essentially important for the optically driven ultrafast spin dynamics. The choice of such a combined basis set within our high-level correlational method has been applied in various large magnetic systems, such as ligand-stabilized complexes [51,52], Ni/Co adsorbed graphene nanoflakes [46,47], and endohedral metallofullerenes [53], and proven to be reliable.

Then, the spin orbit coupling (SOC), the two-electron contributions of which are accounted for by the effective charges [54] and an external static magnetic field (with a strength of  $10^{-5}$  atomic units) are considered. At this stage, the degeneracy of the states are lifted due to the cooperative effects of zero-field splitting and the Zeeman effect, and therefore the different substates from the same triplet terms can be energetically distinguished and explicitly addressed.

Under the influence of the time-dependent laser pulse, the many-body states are propagated as follows:

$$\frac{\partial c_n(t)}{\partial t} = -\frac{i}{\hbar} \sum_k \langle \Psi_n | \hat{H}(t) | \Psi_k \rangle c_k(t) e^{-i(E_k - E_n)t/\hbar}, \quad (1)$$

where  $c_n(t)$  is the coefficient of state  $\Psi_n$ ,  $E_n$  is the energy of it, and  $\hat{H}(t) = \hat{\mathbf{D}} \cdot \mathbf{E}_{\text{laser}}(t)$  with  $\hat{\mathbf{D}}$  being the electric-

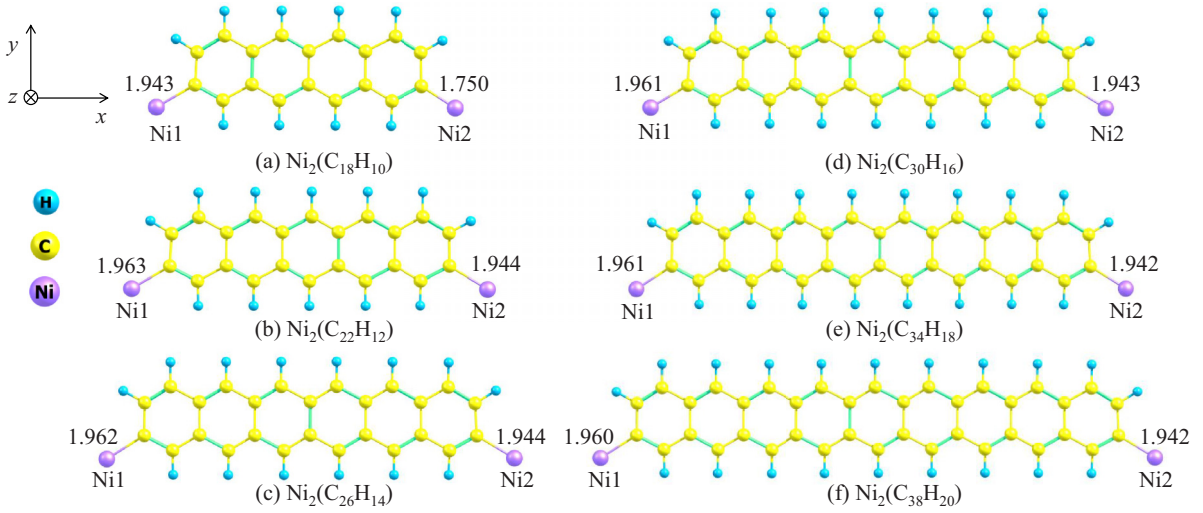


FIG. 1. The optimized geometries of (a)  $\text{Ni}_2(\text{C}_{18}\text{H}_{10})$ , (b)  $\text{Ni}_2(\text{C}_{22}\text{H}_{12})$ , (c)  $\text{Ni}_2(\text{C}_{26}\text{H}_{14})$ , (d)  $\text{Ni}_2(\text{C}_{30}\text{H}_{16})$ , (e)  $\text{Ni}_2(\text{C}_{34}\text{H}_{18})$ , and (f)  $\text{Ni}_2(\text{C}_{38}\text{H}_{20})$ . The two bonds (in Å) between Ni1/Ni2 and the adjacent C for each structure are marked.

dipole-transition operator, and  $\mathbf{E}_{\text{laser}}(t) = \vec{E}_0 e^{i(\vec{k}\cdot\vec{r} - \omega t)}$  being the time-dependent electric field of the laser pulse. By choosing appropriate initial and final states with different magnetic properties, some specified functional spin dynamics (e.g., spin flip for which the initial and final states possess opposite spin directions, spin transfer for which the initial and final states exhibit different spin localizations) are explored through the  $\Lambda$  process (i.e., a two-step transition process consisting of the excitation from the initial state to the intermediate states and the subsequent deexcitation from the intermediate states to the final state) [55]. The equations are numerically solved using the fifth-order Runge-Kutta method combined with the Cash-Karp adaptive step size control [56], and during this step the self-programmed, largely flexible genetic algorithm is applied to effectively optimize the laser parameters (including the laser energy  $E_{\text{laser}}$ , amplitude  $E_0$ , full width at half maximum FWHM, direction angles  $\theta$  and  $\phi$ , and polarization angle  $\gamma$ ) [57]. Here we note that for the linearly polarized laser pulse  $\mathbf{E}_{\text{laser}}(t)$  used in our paper, its energy is given through frequency  $\omega$ , FWHM is determined by the pulse envelope, and the definition of the three angles can be found from the sketch of the coordinate axes adopted in the computation of laser-structure interaction in Ref. [58]. More details about the theoretical method can be found in our previous work [51,59,60].

### III. GEOMETRY AND STRUCTURAL PROPERTIES

The optimized geometries of  $\text{Ni}-(\text{C}_{4n+2}\text{H}_{2n+2})-\text{Ni}$  complexes ( $n = 4 \sim 9$ ) with two distal H atoms substituted by two Ni atoms at the same side obtained at the HF level are shown in Fig. 1. Here we tried both the symmetric and asymmetric configurations (with respect to the bonds C-Ni1 and C-Ni2) and found that except for  $\text{Ni}_2(\text{C}_{22}\text{H}_{12})$ , for which the symmetric configuration (with the bond lengths of C-Ni1 and C-Ni2 equaling 1.871 Å) is lower than the asymmetric case by 0.35 eV, all the other five structures are more stable with asymmetric configurations. Considering the fact that the symmetric configuration of  $\text{Ni}_2(\text{C}_{22}\text{H}_{12})$  does not satisfy the prerequisite of transferring spin in the pursuit of potential

spin functionality due to the indistinguishability of the two magnetic atoms [61], we choose the stable asymmetric configuration of it to demonstrate in this paper. As shown in Fig. 1, all structures exhibit the same symmetry of  $C_s$ , with the C-H bond lengths between 1.082 and 1.091 Å (close to the C-H length of 1.084 Å in benzene). The C-Ni1 and C-Ni2 bonds of almost all structures are in the ranges of 1.960 ~ 1.963 Å and 1.942 ~ 1.944 Å, respectively, indicating the inequality of the two Ni atoms, which can further induce the different spin localization of them (which for sure holds for the shortest structure that exhibits the largest bond difference between the two Ni atoms). We also note that the planar geometry of each  $n$ -acene molecule after substitution with two Ni atoms is not destroyed. This is also the case for Fe( $n$ -acenes)-Fe and Co( $n$ -acenes)-Co, which are not considered due to the symmetric TM-C bonds at the ends of each structure. However, when the two substituted TM atoms are different, the geometry of each  $n$ -acene molecule will be distorted and become nonplanar due to the asymmetry caused by heteronuclear magnetic atoms.

By inspecting the HOMO-LUMO gaps of the six structures (detailed information can be found in the Appendix), we find that the gap values of  $\text{Ni}-(\text{C}_{4n+2}\text{H}_{2n+2})-\text{Ni}$  are 2.402, 2.009, 2.021, 2.068, 2.143, and 2.213 eV, respectively, which keep almost unchanged irrespectively of  $n$ , this is different from the case that the gap of the pure  $\text{C}_{4n+2}\text{H}_{2n+4}$  molecule decreases as  $n$  increases [38]. It should also be noted that, for each structure, the substitution of two Ni atoms makes the HOMO-LUMO energy gap shrink (by about 4 ~ 6 eV) compared to the corresponding  $\text{C}_{4n+2}\text{H}_{2n+4}$  molecule, indicating the property modification by the introduction of magnetic atoms.

We also perform the calculation of the infrared spectra, and find that no imaginary frequency values exist, which thus verifies the stability of the above geometries. In addition, the results show that the spectra features of all six structures exhibit similarly. The frequency values (not scaled) of their normal modes with relatively high intensity are mainly located at three regions: 1321 ~ 1524  $\text{cm}^{-1}$ , 1541 ~ 1981  $\text{cm}^{-1}$ , and 3537 ~ 3731  $\text{cm}^{-1}$ . The spectra in the former two regions correspond to the modes of C-C stretching and C-H in-plane

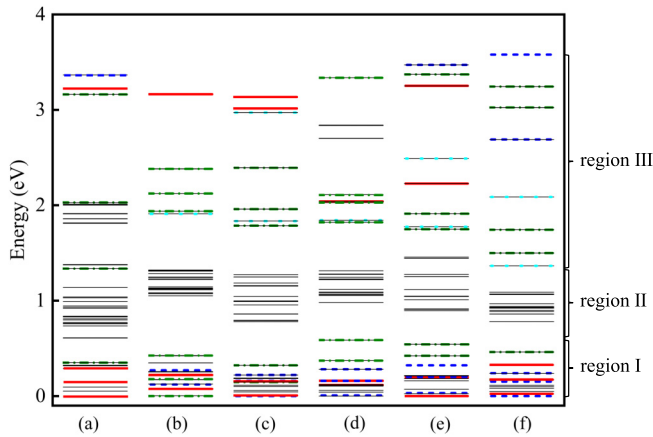


FIG. 2. (a)–(f) Low-lying electronic states of the six structures obtained from the SAC-CI method after the inclusion of SOC and the magnetic field along the  $x$  axis (i.e., along the carbon chain, as shown in Fig. 1). For each structure, the red solid, blue dashed, and cyan dotted lines represent the states with spin singly localized on Ni1, Ni2, and carbon chain, respectively, the green dashed-dotted lines are states with spin doubly localized on both the Ni1/Ni2 atom and carbon chain, and the black solid lines denote the nonlocalized states.

bending, and the third region relates to the C-H stretching. The modes concerning the vibrations between Ni atoms and  $n$ -acene molecules are all below  $600\text{ cm}^{-1}$  with much lower intensity.

#### IV. ELECTRONIC STRUCTURES AND SPIN LOCALIZATION

Based on the HF wave functions, the more accurate electronic states that include correlations are obtained by the subsequent SAC-CI calculation. Each state is constructed by the linear combination of various determinants based on numerous virtual excitations. To help readers understand more clearly, the main single and double virtual excitations (with coefficients above 0.100) that contribute to the ground state for each structure are listed in the Appendix, from which we see that the dominant determinant (the one with the largest coefficient) for each ground state comes from single excitation. However, this does not mean the double excitations with smaller coefficients are trivial because they can prevail with the large amount of related determinant terms.

Figure 2 shows the lowest 61 ground and excited states of the six structures obtained by the SAC-CI method after the inclusion of SOC and an external magnetic field along the  $x$  axis. The level distributions for the magnetic field along the  $y$  or  $z$  axis are almost the same as Fig. 2 since the direction hardly affects the energy values of the states, and thus are not shown here. Clearly, within the calculation window, the level expansions of six structures are all below 4 eV and overall locate similarly in three regions: the concentratively distributed region below 0.61 eV (region I), the region ranging from 0.74 to 1.35 eV (region II), and the dispersively distributed region above 1.36 eV (region III). Here, the classification of these three regions is not merely based on the energy location of the states but also their spin localization features (see the later discussion).

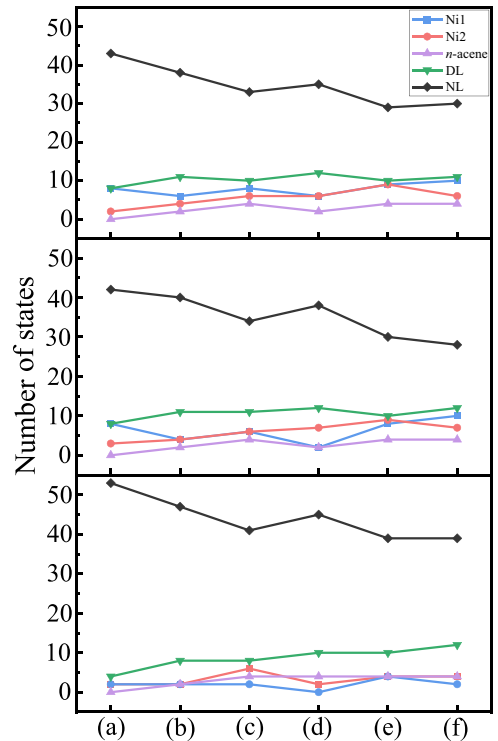


FIG. 3. The number of five types of different spin-localized states for each structure under B field in the  $x$  (a),  $y$  (b), and  $z$  (c) directions, respectively.

Although the level distributions of the structures are independent on the magnetic-field (B-field in short) direction, the spin localization of them is quite closely related to the B-field direction due to the anisotropic nature of the structures and exhibits different features. Here, we plot the detailed spin localization of the six structures under three B-field directions of  $x$ ,  $y$ , and  $z$  axes in Fig. 3. For each of the structures, the states are divided into five categories according to the Mulliken spin-density values: states with a spin singly localized (with spin-density value on single atom (or  $n$ -acene molecule) above 1.2 and percentage value above 80% of the total density value) on Ni1, Ni2, and  $C_{4n+2}H_{2n+2}$ , respectively, states with spin doubly localized (with the sum of the two almost equal spin-density values above 1.2 and percentage value above 80% of the total density value) on two parts (abbreviated by DL), and the nonlocalized spin states (abbreviated by NL). As can be seen in Fig. 3, the spin localization of each structure when the B field is applied along the  $x$  direction is similar to that when the field is along the  $y$  axis (however, note here that it does not mean the localized states are correspondingly the same). While for the case when the magnetic field is applied perpendicularly to the structural plane (i.e., the  $z$  axis), the amount of the singly localized states on Ni atoms noticeably decreases and the amount of the nonlocalized states increases. It should be noted that, except for  $Ni_2(C_{18}H_{10})$ , all the other structures possess a certain fixed amount of states with spin localized on  $n$ -acene molecule. This strong spin localization on the carbon chain bridges, which has not been especially concerned in our previous investigation of carbon-based magnetic structures [44,46,62], can provide additional channels

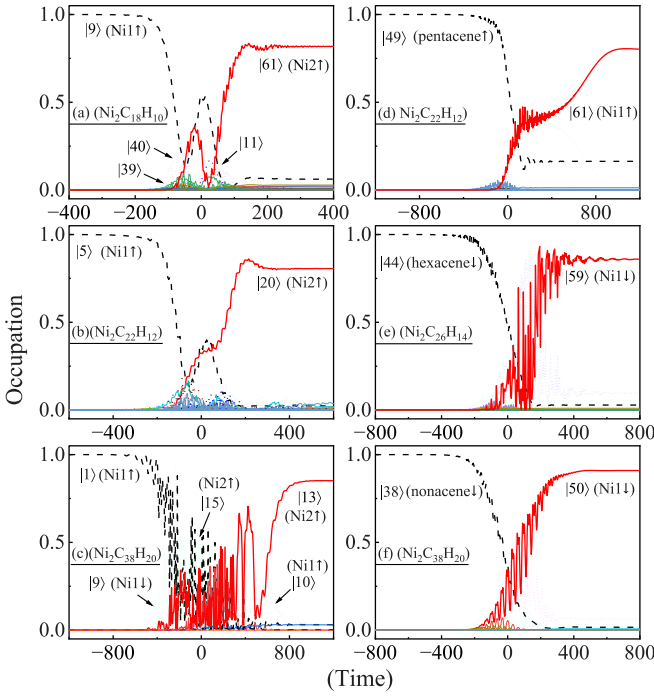


FIG. 4. Ultrafast spin-transfer scenarios achieved in (a)  $\text{Ni}_2(\text{C}_{18}\text{H}_{10})$  ( $|9\rangle \rightarrow |61\rangle$ ), (b)  $\text{Ni}_2(\text{C}_{22}\text{H}_{12})$  ( $|5\rangle \rightarrow |20\rangle$ ), (c)  $\text{Ni}_2(\text{C}_{38}\text{H}_{20})$  ( $|11\rangle \rightarrow |13\rangle$ ), (d)  $\text{Ni}_2(\text{C}_{22}\text{H}_{12})$  ( $|49\rangle \rightarrow |61\rangle$ ), (e)  $\text{Ni}_2(\text{C}_{26}\text{H}_{14})$  ( $|44\rangle \rightarrow |59\rangle$ ), (f)  $\text{Ni}_2(\text{C}_{38}\text{H}_{20})$  ( $|38\rangle \rightarrow |50\rangle$ ). In each panel, the black dashed, red solid, and dotted lines represent the time-resolved occupations of the initial, final, and intermediate states, respectively.

for spin and charge transfer and thus holds much promise in future spin logic and quantum circuit. In addition, as the carbon chain length becomes longer, the summed amount of the states with spin localization on Ni atoms increases irrespectively of the direction of the magnetic field. For the case when the magnetic field is along the  $z$  axis, the amount of the states with spin localized on carbon chain for the latter four structures keeps unchanged with the increase of benzene rings.

TABLE I. Information of the initial and final states (including their energies, spin expectation values, spin density, and charge density) of the  $\Lambda$  processes shown in Fig. 4.

| Structure                                 | Initial/final states | Energy (eV) | Spin components       |                       |                       | Spin density |       |            | Charge density |        |            |
|---|----------------------|-------------|-----------------------|-----------------------|-----------------------|--------------|-------|------------|----------------|--------|------------|
|   |                      |             | $\langle S_x \rangle$ | $\langle S_y \rangle$ | $\langle S_z \rangle$ | Ni1          | Ni2   | $n$ -acene | Ni1            | Ni2    | $n$ -acene |
| $\text{Ni}_2(\text{C}_{18}\text{H}_{10})$ | $ 9\rangle$          | 0.292       | 0.828                 | 0.2751                | 0.000                 | 0.008        | 1.751 | 0.055      | -0.278         | -0.601 | 0.879      |
|   | $ 61\rangle$         | 3.367       | 0.846                 | 0.246                 | 0.000                 | 1.464        | 0.010 | 0.382      | -0.244         | -0.639 | 0.882      |
| $\text{Ni}_2(\text{C}_{22}\text{H}_{12})$ | $ 5\rangle$          | 0.075       | 0.637                 | 0.361                 | 0.000                 | 1.459        | 0.001 | 0.047      | -0.501         | -0.614 | 1.115      |
|   | $ 20\rangle$         | 0.270       | -0.773                | 0.525                 | 0.000                 | 0.000        | 1.855 | 0.063      | -0.543         | -0.570 | 1.113      |
| $\text{Ni}_2(\text{C}_{38}\text{H}_{20})$ | $ 11\rangle$         | 0.000       | -0.698                | -0.377                | 0.000                 | 1.568        | 0.000 | 0.056      | -0.540         | -0.654 | 1.194      |
|   | $ 13\rangle$         | 0.172       | -0.740                | 0.533                 | 0.000                 | 0.000        | 1.791 | 0.064      | -0.586         | -0.595 | 1.181      |
| $\text{Ni}_2(\text{C}_{22}\text{H}_{12})$ | $ 49\rangle$         | 1.910       | 0.747                 | -0.441                | 0.000                 | 0.288        | 0.021 | 1.528      | -0.314         | -0.594 | 0.908      |
|   | $ 61\rangle$         | 3.165       | 0.940                 | -0.001                | 0.000                 | 1.731        | 0.018 | 0.190      | -0.359         | -0.632 | 0.990      |
| $\text{Ni}_2(\text{C}_{26}\text{H}_{14})$ | $ 44\rangle$         | 1.834       | -0.909                | -0.033                | 0.000                 | 0.034        | 0.022 | 1.849      | -0.594         | -0.567 | 1.161      |
|   | $ 59\rangle$         | 3.134       | -0.684                | 0.022                 | 0.000                 | 1.588        | 0.007 | 0.059      | -0.529         | -0.629 | 1.158      |
| $\text{Ni}_2(\text{C}_{38}\text{H}_{20})$ | $ 38\rangle$         | 1.364       | -0.921                | 0.052                 | 0.000                 | 0.007        | 0.006 | 1.908      | -0.587         | -0.649 | 1.235      |
|   | $ 50\rangle$         | 2.689       | -0.914                | 0.134                 | 0.000                 | 1.735        | 0.003 | 0.183      | -0.428         | -0.657 | 1.085      |

One can also notice from Fig. 2 that the states with spin singly localized on Ni1 or Ni2 (red solid and blue dashed lines) mainly concentratively locate in region I, region II accommodates only the nonlocalized states (black solid lines), and all the states with spin singly localized on linearly fused benzene rings (cyan dotted lines) lie in region III. For instance, for the longest structure  $\text{Ni}_2(\text{C}_{38}\text{H}_{20})$ , among all the 16 states with spin singly localized on Ni1/Ni2, 75% of them lie in region I, 13 out of 30 nonlocalized states are in region II as the unique localization type, and all four states with spin singly localized on carbon chain are in region III. Especially, for region I, detailed inspection shows that the level interspersing for such chainlike  $\pi$  conjugated systems is quite strong (see the latter discussion). All these features will affect the choice of the candidate initial and final states for certain spin dynamics and thus the realization of the related spin functionality, as discussed in the next section.

## V. ULTRAFAST SPIN TRANSFER DYNAMICS

For the realization of spin logic functionality and information transmission towards spintronic devices application, in addition to the function of spin flip (which has been achieved in all of these structures), the ability of transmitting spin from one site to another site (through the spin-transfer dynamics) is also one significant and indispensable prerequisite. In this section, three types of spin-transfer scenarios will be discussed, i.e., (1)  $\text{Ni1} \leftrightarrow \text{Ni2}$ , (2)  $\text{Ni1/Ni2} \leftrightarrow \text{C}_{4n+2}\text{H}_{2n+2}$ , and (3)  $\text{Ni1} \leftrightarrow \dots \leftrightarrow \text{Ni2}$ . Here,  $\leftrightarrow \dots \leftrightarrow$  means the indirect spin transfer between Ni1 and Ni2 facilitated by several bridging  $\Lambda$  processes.

For the first type, the transfer between a state with spin localization on Ni1 and a state with spin localization on Ni2 is achieved in three structures, i.e.,  $\text{Ni}_2(\text{C}_{18}\text{H}_{10})$ ,  $\text{Ni}_2(\text{C}_{22}\text{H}_{12})$ , and  $\text{Ni}_2(\text{C}_{38}\text{H}_{20})$ , as shown Figs. 4(a)–4(c). Here, we take Fig. 4(a) as an example to illustrate the spin-transfer scenario in detail. The initial and final states are states  $|9\rangle$  (with spin localization on Ni1 since the spin-density values on Ni1, Ni2, and naphthacene are 1.751, 0.008, and 0.055, respectively) and  $|61\rangle$  (with spin localization on Ni2 since the spin-density

TABLE II. The parameters of the optimized laser pulses for the ultrafast spin-transfer scenarios in Fig. 4. Here  $\theta$  and  $\phi$  denote the angles of the incidence in spherical coordinates,  $\gamma$  is the angle between the polarization of the light and the optical plane, and FWHM is the full width at half maximum of the laser pulse. For each process, the localization change, the energy difference between the initial and final states, and the fidelity value are also given.

| $\Lambda$ process  | Localization change              | Fidelity (%) | $E_{\text{final}} - E_{\text{initial}}$ (eV) | Laser parameters        |                  |           |                |              |                |
|--|----------------------------------|--------------|--|-------------------------|------------------|-----------|----------------|--------------|----------------|
|  |                                  |              |  | $E_{\text{laser}}$ (eV) | Amplitude (a.u.) | FWHM (fs) | $\theta$ (deg) | $\phi$ (deg) | $\gamma$ (deg) |
| $\Lambda 1$ Ni <sub>2</sub> (C <sub>18</sub> H <sub>10</sub> ) | 9⟩ (Ni1 ↑) →  61⟩ (Ni2 ↑)        | 81.8         | 3.074  | 1.030                   | 0.0086           | 326.4     | 22.8           | 66.8         | 183.4          |
| $\Lambda 2$ Ni <sub>2</sub> (C <sub>22</sub> H <sub>12</sub> ) | 5⟩ (Ni1 ↑) →  20⟩ (Ni2 ↑)        | 81.8         | 0.195  | 0.200                   | 0.0083           | 472.2     | 269.0          | 316.9        | 157.6          |
| $\Lambda 3$ Ni <sub>2</sub> (C <sub>38</sub> H <sub>20</sub> ) | 1⟩ (Ni1 ↓) →  13⟩ (Ni2 ↓)        | 85.1         | 0.172  | 0.040                   | 0.0084           | 478.9     | 25.5           | 68.8         | 247.0          |
| $\Lambda 4$ Ni <sub>2</sub> (C <sub>22</sub> H <sub>12</sub> ) | 49⟩ (pentacene ↑) →  61⟩ (Ni1 ↑) | 80.2         | 1.254  | 1.048                   | 0.0059           | 478.9     | 95.0           | 258.8        | 46.5           |
| $\Lambda 5$ Ni <sub>2</sub> (C <sub>26</sub> H <sub>14</sub> ) | 44⟩ (hexacene ↓) →  59⟩ (Ni1 ↓)  | 85.9         | 1.300  | 1.300                   | 0.0081           | 428.0     | 83.7           | 29.4         | 204.2          |
| $\Lambda 6$ Ni <sub>2</sub> (C <sub>38</sub> H <sub>20</sub> ) | 38⟩ (nonacene ↓) →  50⟩ (Ni1 ↓)  | 90.9         | 1.325  | 1.310                   | 0.0091           | 350.2     | 289.0          | 46.7         | 29.1           |

values on Ni1, Ni2, and naphthacene are 0.010, 1.464, and 0.382, respectively), respectively, the detailed information of which can be found in Table I. Under the influence of the appropriate laser pulses (the parameters of which are given in Table II), the occupation probability of the initial state |9⟩ gradually decreases down to 0%, and the occupation probability of the final state |61⟩ gradually increases up to 81.8%, which indicates the spin transfer from Ni1 to Ni2 is achieved. The whole process lasts around 0.4 ps, which is determined by the time duration between when the probability of the initial state starts to decrease and when the final state starts to achieve the desired steady probability. Here we note that this time duration is not merely determined by the laser duration (which relates to laser parameter FWHM, and smaller FWHM. e.g., 100 fs, normally achieves faster dynamics than the one with larger FWHM, e.g., 500 fs), but also affected by the involvement of the intermediate states (especially for the cases when the FWHM values are close to each other) since more intermediate states can give rise to more strong oscillations and complexities and thus slow down the process. This can be clearly seen from Figs. 4(c) and 4(d). The detailed information of the involved initial and final states in the other two scenarios can be found in Table I.

Although candidate initial and final states with different spin localizations on magnetic atoms exist in other structures,

due to the absence of appropriate intermediate states or unbalanced transitions of the two branches of the  $\Lambda$  process to facilitate [61], this type of spin transfer has not been found within our calculated energy window. Another non-negligible reason in some cases comes from the fact that there exists strong level interspersing of states (due to the cooperative effects of SOC and dense energy distribution) originating from different triplet terms. Here, we take one of the failed spin-transfer scenarios for structure Ni<sub>2</sub>(C<sub>30</sub>H<sub>16</sub>) as an example to illustrate, as shown in Fig. 5(a). The candidate initial and final states are chosen as states |12⟩ (with spin localization on Ni2) and |13⟩ (with spin localization on Ni1), respectively. Clearly, after the propagation the system does not go to the targeted state |13⟩ but mainly ends up with a linear combination of states |12⟩ and |14⟩. The absorption spectra of the candidate initial and final states are shown in Fig. 5(b), in which the abscissa denotes the energy positions of the 61 states for structure Ni<sub>2</sub>(C<sub>30</sub>H<sub>16</sub>), the ordinate represents the oscillator strength (in logarithmic scale with arbitrary units [51] with a Gaussian broadening of 0.01 eV), and the existence of the peaks indicates that the allowed transitions occur between the specified states (either the initial or the final states) and the other states (i.e., intermediate states). One can see that there indeed exist several common intermediate states that have both transitions with states |12⟩ and |13⟩ in the energy region

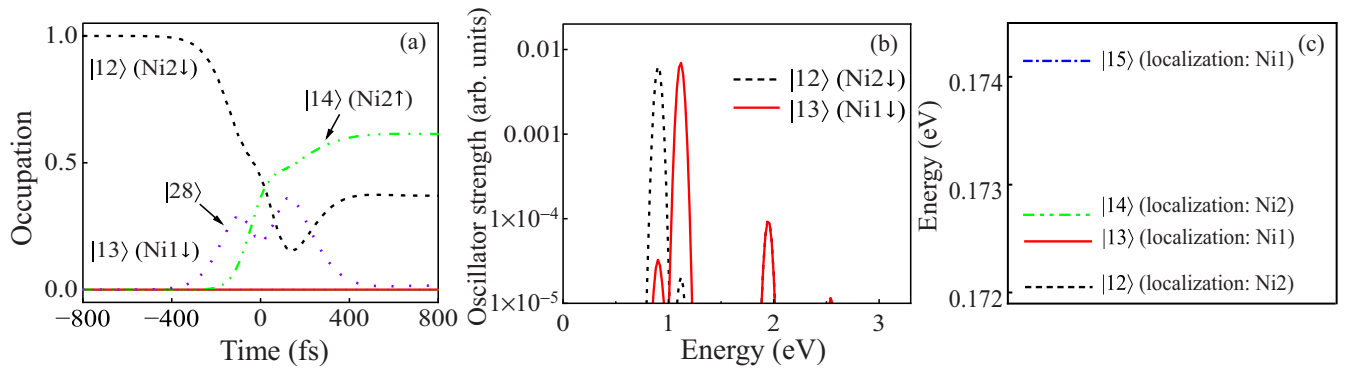


FIG. 5. The analysis of the failure of the transfer scenarios for the first type during region I. (a) Absorption spectra of states |12⟩ and |13⟩ for Ni<sub>2</sub>(C<sub>30</sub>H<sub>16</sub>). (b) Time-resolved occupation of the involved states for the dynamics with states |12⟩ and |13⟩ as the initial and final states, respectively. (c) Magnification of the levels in the range of 0.1719 ~ 0.1745 eV with the states and the localization for spin-localized states clearly marked.

of 0.92 ~ 1.12 eV, however, their strengths differ by more than two orders of magnitude, which brings about difficulties for the realization of the corresponding transfer dynamics via the  $\Lambda$  process. To see how the dynamics goes to state  $|14\rangle$  instead of  $|13\rangle$ , we magnify its energy region of 0.17207 ~ 0.17432 eV to inspect the level interspersing in detail. As shown in Fig. 5(c), substates  $|12\rangle$  and  $|14\rangle$  (originate from the fourth triplet term) and substates  $|13\rangle$  and  $|15\rangle$  (originate from the fifth triplet term) are closely interlaced, with the time evolution the system prefers to reach state  $|14\rangle$  (which corresponds to spin flip) rather than  $|13\rangle$  (which corresponds to spin transfer). The reason is that the  $\Lambda$  process is more easily realized if its two branches are symmetric [61], especially for the case of  $|i_{m_s=1}\rangle \leftrightarrow |f_{m_s=-1}\rangle$  with the initial and final states originating from the same triplet term but possessing opposite spin directions under the participation of several intermediate states  $|inter_{m_s=1,0,-1}\rangle$  (without which the direct transition is optically forbidden within the electric dipole approximation). We also note here that for the two states which are energetically close enough, this indirect transition channel (i.e., the  $\Lambda$ ) can also be faster compared to the direct transition.

For the level interspersing phenomenon in these structures, trials of decreasing the strength of the external magnetic field also have been made. However, it shows that the crossing still exists even when the field strength goes down to  $10^{-8}$  a.u. (note here that the field strength smaller than this value cannot distinguish spin-up and spin-down states anymore because of the negligible Zeeman splitting). The same situation also appears in carbon chain structures [44]. We attribute this to the intrinsic nature of this kind of fused linear structures since usually chainlike structures possess high symmetry (although reduced by the introduction of magnetic atoms), which can bring about higher degeneracy of the states.

For the second type, the spin transfer between Ni1 (the one has a longer Ni-C bond of 1.96 Å compared to Ni2) and  $C_{4n+2}H_{2n+2}$  molecules is obtained in structures  $Ni_2(C_{22}H_{12})$ ,  $Ni_2(C_{26}H_{14})$ , and  $Ni_2(C_{38}H_{20})$ , as shown in Figs. 4(d)–4(f). As mentioned previously, these structures possess spin-localized states on  $n$ -acene molecule. The realization of such a transfer scenario is believed to be promising in carbon-based spintronics since the long-distance carbon chain serves as spin communication transmitting spin flows like currents in an electronic circuit.

It should be noted that, usually, the laser energy for spin transfer is largely determined by the energy difference between the initial and final states, which is true for processes  $\Lambda_2$ ,  $\Lambda_4$ ,  $\Lambda_5$ , and  $\Lambda_6$  listed in Table II. Here, the laser energies are noticeably lower for processes  $\Lambda_1$  and  $\Lambda_3$ . The reasons can be attributed to the involvement of several intermediate states with relatively high occupation probabilities during the evolution process that enables the whole scenario undergoes a  $\Xi$  type [61] or multistep type transition with respect to the energies of the states. For instance, for process  $\Lambda_1$ , the main intermediate states are states  $|39\rangle$  and  $|40\rangle$  [as indicated by Fig. 4(a)] with energies around 1.340 eV (which is almost half of the energy difference  $|E_{|61\rangle} - E_{|9\rangle}|$ ), the transition from the initial state  $|9\rangle$  to these two main intermediate states and the subsequent ascending transition from them to the final state  $|61\rangle$  leading to the laser energy being around 1 eV instead of 3 eV. Similarly, the main intermediate states sequentially

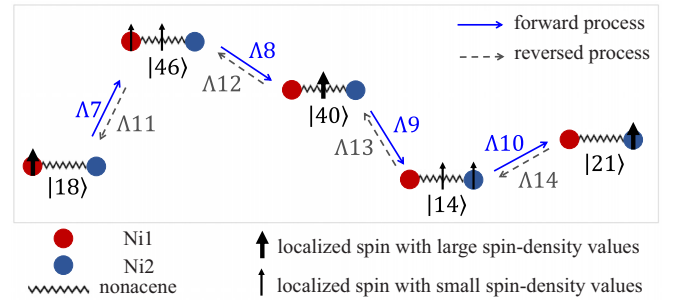


FIG. 6. Illustration of the four  $\Lambda$  processes that enable the realization of spin transfer from Ni1 to Ni2 in structure  $Ni_2(C_{38}H_{20})$ . Here, the information of the initial and final states, including the spin localization and the relative energy location, are shown. The laser parameters of the corresponding  $\Lambda$  processes can be found in Table V.

involved in process  $\Lambda_3$  are states  $|9\rangle$ ,  $|15\rangle$ , and  $|10\rangle$  with energies 0.150, 0.154, 0.152 eV, respectively, this population transfer pathway, although complicated in behavior, giving rise to a smaller laser detuning and thus a relatively low laser energy.

We find that, in some cases, the transfer between candidate initial and final states with spin localizations on different Ni atoms cannot be achieved through one  $\Lambda$  process but several bridging  $\Lambda$  processes (which correspond to the third transfer type). This opens an additional path for realizing the desired spin functionality. As an example, we show the diagram of such a spin-transfer type achieved in  $Ni_2(C_{38}H_{20})$  in Fig. 6, from which one can clearly see the transfer from Ni1 to Ni2 can be achieved through four steps, i.e., spin bifurcation (denoted by  $\Lambda_7$ ) from state  $|18\rangle$  (Ni1) to state  $|46\rangle$  (Ni1 and nonacene), spin merging (denoted by  $\Lambda_8$ ) from state  $|46\rangle$  (Ni1 and nonacene) to state  $|40\rangle$  (nonacene), spin bifurcation (denoted by  $\Lambda_9$ ) from state  $|40\rangle$  (nonacene) to state  $|14\rangle$  (nonacene and Ni2), and spin merging (denoted by  $\Lambda_{10}$ ) from state  $|14\rangle$  (nonacene and Ni2) to state  $|21\rangle$  (Ni2). The laser parameters of these four processes together can be found in Table V, from which one can also see that the fidelity values are 96.8%, 100.0%, 98.4%, and 99.9%, respectively, contributing a total efficiency of 98.2%. The total time duration of the whole process is found to be 2.15 ps. Interestingly, the four scenarios turn out to all be reversible (under different laser pulses from the respective forward processes, as listed in Table V), with the fidelity of 96.6%, 99.8%, 94.2%, and 93.2%, respectively. Detailed inspection shows that, in each process, electron transfer between different parts occurs, accompanied with the spin-density transfer. Especially, for the spin merging process  $\Lambda_8$  ( $|46\rangle \rightarrow |40\rangle$ ), the charge-density values on Ni1, Ni2, and nonacene change from 0.333,  $-0.654$  and 0.321 to  $-0.587$ ,  $-0.649$ , and 1.235, respectively, indicating that an electron is transferred from nonacene to Ni1. Clearly, the electron-transfer direction is opposite to the spin-transfer direction (i.e., Ni1  $\rightarrow$  nonacene) of this process. The same situation also occurs for the spin bifurcation process  $\Lambda_9$  ( $|40\rangle \rightarrow |14\rangle$ ), in which the electron is transferred from Ni2 to nonacene whereas the spin density transfer is from nonacene to Ni2 (details can be found in Table III). This feature combined with the reversibility provides richer options

TABLE III. Information of the initial and final states (including their energies, spin expectation values, spin density, and charge density) of the  $\Lambda$  processes involving in Fig. 6 and Table IV.

| Initial/final states | Energy (eV) | Spin components       |                       |                       | Spin density |       |                 | Charge density |        |                 |
|----------------------|-------------|-----------------------|-----------------------|-----------------------|--------------|-------|-----------------|----------------|--------|-----------------|
|                      |             | $\langle S_x \rangle$ | $\langle S_y \rangle$ | $\langle S_z \rangle$ | Ni1          | Ni2   | <i>n</i> -acene | Ni1            | Ni2    | <i>n</i> -acene |
| 1⟩                   | 0.000       | -0.698                | -0.377                | 0.000                 | 1.568        | 0.000 | 0.056           | -0.540         | -0.654 | 1.194           |
| 9⟩                   | 0.150       | -0.772                | -0.428                | 0.000                 | 1.742        | 0.000 | 0.065           | -0.542         | -0.654 | 1.192           |
| 14⟩                  | 0.173       | 0.868                 | -0.049                | 0.000                 | 0.003        | 0.931 | 0.931           | -0.588         | 0.264  | 0.325           |
| 17⟩                  | 0.240       | -0.695                | -0.600                | 0.000                 | 1.861        | 0.000 | 0.051           | -0.568         | -0.664 | 1.222           |
| 18⟩                  | 0.240       | 0.851                 | 0.342                 | 0.000                 | 1.861        | 0.000 | 0.051           | -0.568         | -0.664 | 1.222           |
| 21⟩                  | 0.328       | 0.693                 | -0.395                | 0.000                 | 0.000        | 1.635 | 0.027           | -0.585         | -0.665 | 1.250           |
| 22⟩                  | 0.461       | -0.805                | 0.292                 | 0.000                 | 0.963        | 0.000 | 0.876           | 0.247          | -0.654 | 0.407           |
| 24⟩                  | 0.463       | 0.805                 | 0.174                 | 0.000                 | 0.926        | 0.000 | 0.843           | 0.247          | -0.654 | 0.407           |
| 38⟩                  | 2.689       | -0.914                | 0.134                 | 0.000                 | 1.735        | 0.003 | 0.183           | -0.428         | -0.657 | 1.085           |
| 40⟩                  | 1.365       | 0.921                 | -0.051                | 0.000                 | 0.007        | 0.006 | 1.908           | -0.587         | -0.649 | 1.235           |
| 46⟩                  | 1.744       | 0.853                 | 0.011                 | 0.000                 | 0.930        | 0.000 | 0.915           | 0.333          | -0.654 | 0.321           |
| 47⟩                  | 2.087       | -0.890                | 0.033                 | 0.000                 | 0.034        | 0.006 | 1.847           | -0.586         | -0.648 | 1.234           |
| 49⟩                  | 2.088       | 0.888                 | -0.067                | 0.000                 | 0.034        | 0.006 | 1.847           | -0.586         | -0.648 | 1.234           |
| 50⟩                  | 2.689       | -0.914                | 0.134                 | 0.000                 | 1.735        | 0.003 | 0.183           | -0.428         | -0.657 | 1.085           |
| 52⟩                  | 2.690       | 0.922                 | 0.030                 | 0.000                 | 1.733        | 0.003 | 0.183           | -0.428         | -0.657 | 1.085           |

for the construction of various spin functionalities and thus enables the related structure to be of great potential in future device applications.

## VI. SPIN LOGIC GATE

For the practical applications in quantum computing, demonstrating spin logic functionality is of utmost significance. Previously, we have proposed the ERASE functionality for the quasilinear molecular ions  $[\text{Fe}-\text{O}-\text{Co}]^+$  based on the achieved laser-induced spin-flip and -transfer scenarios combined with the irreversible features [58]. Exploiting the appropriate spin states of several spin scenarios as input and output bits, some two-qubit logic gates are constructed in a  $\pi$ -conjugated  $\text{Co}_4$ -GNF structure [47]. Aiming at offering wider flexibility to process quantum information, a universal set of quantum gates controlled by suitably tailored femtosecond laser pulses has also been built in a heteronuclear  $3d-4f$   $[\text{Dy}_2\text{Ni}_2]$  real molecular magnet [63].

In this paper, based on the achieved spin scenarios, we are also able to construct several elementary logic gates. Here, we take the scenarios obtained in  $\text{Ni}_2(\text{C}_{38}\text{H}_{20})$  as examples to demonstrate how to build the related functionality. First comes the SWAP gate. Here, the two-bit state is defined according

to the spin localization (localization on nonacene represents 1, and localization on Ni1 represents 0) and spin direction (spin up denotes 1 and spin down denotes 0). For instance, the spin state  $|\text{nonacene } \uparrow\rangle$  corresponds to the bit 11, and  $|\text{Ni1 } \downarrow\rangle$  corresponds to the bit 00. With the assistance of several specialized scenarios, the whole SWAP function can be realized, as shown in the upper part of Table IV. Due to the failure of spin transfer between states with different spin localizations (i.e., nonacene and Ni1) and opposite spin directions through one  $\Lambda$  process, two successive  $\Lambda$  processes (i.e., spin-flip scenario and subsequent spin-transfer scenario) are needed to realize the transfer from  $|\text{nonacene } \downarrow\rangle$  to  $|\text{Ni1 } \uparrow\rangle$  or the transfer from  $|\text{Ni1 } \uparrow\rangle$  to  $|\text{nonacene } \downarrow\rangle$ .

Another logic gate is the XOR, the construction of which is shown in the lower part of Table IV. Here, the bit definition of the input states is the same as that for the SWAP gate. However, the spin localization of the output state is confined to be neither on Ni1 nor nonacene, but equally on Ni1 and nonacene (i.e., double localization Ni and nonacene) without carrying any bit information, which thus enables us to focus on the spin direction as the only bit carrier (spin up for 1, and spin down for 0) for the output. For instance, for the input state  $|17\rangle$  (bit 00, since it's a spin-down state with localization on Ni1),

 TABLE IV. Constructions of the SWAP and XOR logic gates for the structure  $\text{Ni}_2(\text{C}_{38}\text{H}_{20})$  based on the achieved spin scenarios.

|      | Input     | $ \text{nonacene } \uparrow\rangle$ (bit 1 1)         | $ \text{nonacene } \downarrow\rangle$ (bit 1 0)  | $ \text{Ni1 } \uparrow\rangle$ (bit 0 1)   | $ \text{Ni1 } \downarrow\rangle$ (bit 0 0)   |
|------|-----------|---|--|--|--|
|      | Output    | $ \text{nonacene } \uparrow\rangle$ (bit 1 1)         | $ \text{Ni1 } \uparrow\rangle$ (bit 0 1)   | $ \text{nonacene } \downarrow\rangle$ (bit 1 0)  | $ \text{Ni1 } \downarrow\rangle$ (bit 0 0)   |
| SWAP | Process   | $ 40\rangle \xrightarrow{\Lambda_{15}}  49\rangle$    | $ 47\rangle \xrightarrow{\Lambda_{16}}  49\rangle \xrightarrow{\Lambda_{17}}  52\rangle$ | $ 52\rangle \xrightarrow{\Lambda_{18}}  50\rangle \xrightarrow{\Lambda_{19}}  38\rangle$ | $ 1\rangle \xrightarrow{\Lambda_{20}}  9\rangle$   |
|      | Time (ps) | 0.300   | 1.250  | 1.165  | 0.960  |
|      | Fidelity  | 99.9%   | 89.1%  | 94.9%  | 100.0%   |
|      | Input     | $ \text{Ni1 } \downarrow\rangle$ (bit 0 0)            | $ \text{Ni1 } \uparrow\rangle$ (bit 0 1)   | $ \text{nonacene } \downarrow\rangle$ (bit 1 0)  | $ \text{nonacene } \uparrow\rangle$ (bit 1 1)  |
|      | Output    | $ \text{Ni1 and nonacene } \downarrow\rangle$ (bit 0) | $ \text{Ni1 and nonacene } \uparrow\rangle$ (bit 1)                                      | $ \text{Ni1 and nonacene } \uparrow\rangle$ (bit 1)                                      | $ \text{Ni1 and nonacene } \downarrow\rangle$ (bit 0)                                    |
| XOR  | Process   | $ 17\rangle \xrightarrow{\Lambda_{21}}  22\rangle$    | $ 18\rangle \xrightarrow{\Lambda_{22}}  24\rangle$                                       | $ 47\rangle \xrightarrow{\Lambda_{16}}  49\rangle \xrightarrow{\Lambda_{23}}  24\rangle$ | $ 49\rangle \xrightarrow{\Lambda_{24}}  47\rangle \xrightarrow{\Lambda_{25}}  22\rangle$ |
|      | Time (ps) | 0.600   | 0.750  | 1.350  | 0.665  |
|      | Fidelity  | 98.3%   | 97.7%  | 89.1%  | 88.5%  |

TABLE V. The laser parameters of the  $\Lambda$  processes in Fig. 6 and Table IV. Here  $\theta$  and  $\phi$  denote the angles of the incidence in spherical coordinates,  $\gamma$  is the angle between the polarization of the light and the optical plane, and FWHM is the full width at half maximum of the laser pulse. For each process, the localization change and fidelity value are also given.

| $\Lambda$ process | Localization change   | Fidelity (%) | $E_{\text{final}}-E_{\text{initial}}$ (eV) | Laser parameters        |                  |           |                |              |                |
|-------------------|---|--------------|--|-------------------------|------------------|-----------|----------------|--------------|----------------|
|                   |   |              |  | $E_{\text{laser}}$ (eV) | Amplitude (a.u.) | FWHM (fs) | $\theta$ (deg) | $\phi$ (deg) | $\gamma$ (deg) |
| $\Lambda 7$       | $ 18\rangle$ (Ni1 $\uparrow$ ) $\rightarrow$ $ 46\rangle$ (Ni1 and nonacene $\uparrow$ )          | 96.8         | 1.504                                      | 1.621                   | 0.0095           | 156.2     | 341.0          | 250.3        | 106.1          |
| $\Lambda 8$       | $ 46\rangle$ (Ni1 and nonacene $\uparrow$ ) $\rightarrow$ $ 40\rangle$ (nonacene $\uparrow$ )     | 100.0        | 0.379                                      | 0.378                   | 0.0032           | 452.1     | 270.0          | 176.3        | 192.1          |
| $\Lambda 9$       | $ 40\rangle$ (nonacene $\uparrow$ ) $\rightarrow$ $ 14\rangle$ (Ni2 and nonacene $\uparrow$ )     | 98.4         | 1.193                                      | 1.257                   | 0.0076           | 259.4     | 290.3          | 81.2         | 227.0          |
| $\Lambda 10$      | $ 14\rangle$ (Ni2 and nonacene $\uparrow$ ) $\rightarrow$ $ 21\rangle$ (Ni2 $\uparrow$ )          | 99.7         | 0.155                                      | 1.312                   | 0.0099           | 495.8     | 149.7          | 324.8        | -35.2          |
| $\Lambda 11$      | $ 46\rangle$ (Ni1 and nonacene $\uparrow$ ) $\rightarrow$ $ 18\rangle$ (Ni1 $\uparrow$ )          | 96.6         | 0.155                                      | 1.692                   | 0.0099           | 368.7     | 266.2          | 98.4         | -252.1         |
| $\Lambda 12$      | $ 40\rangle$ (nonacene $\uparrow$ ) $\rightarrow$ $ 46\rangle$ (Ni1 and nonacene $\uparrow$ )     | 99.8         | 1.193                                      | 1.188                   | 0.0082           | 216.6     | 489.5          | 315.1        | -37.3          |
| $\Lambda 13$      | $ 14\rangle$ (Ni2 and nonacene $\uparrow$ ) $\rightarrow$ $ 40\rangle$ (nonacene $\uparrow$ )     | 94.2         | 0.379                                      | 0.154                   | 0.0093           | 472.3     | -92.3          | 251.3        | -180.5         |
| $\Lambda 14$      | $ 21\rangle$ (Ni2 $\uparrow$ ) $\rightarrow$ $ 14\rangle$ (Ni2 and nonacene $\uparrow$ )          | 93.2         | 1.504                                      | 1.553                   | 0.0068           | 450.1     | 96.4           | 128.9        | 147.7          |
| $\Lambda 15$      | $ 40\rangle$ (nonacene $\uparrow$ ) $\rightarrow$ $ 49\rangle$ (nonacene $\uparrow$ )             | 99.9         | 0.723                                      | 0.354                   | 0.0023           | 237.9     | 81.7           | 96.7         | 346.6          |
| $\Lambda 16$      | $ 47\rangle$ (nonacene $\downarrow$ ) $\rightarrow$ $ 49\rangle$ (nonacene $\uparrow$ )           | 89.1         | 0.001                                      | 0.178                   | 0.0049           | 476.5     | 2.7            | 302.8        | 137.1          |
| $\Lambda 17$      | $ 49\rangle$ (nonacene $\uparrow$ ) $\rightarrow$ $ 52\rangle$ (Ni1 $\uparrow$ )                  | 100.0        | 0.602                                      | 0.378                   | 0.0032           | 452.1     | 269.7          | 176.3        | 192.1          |
| $\Lambda 18$      | $ 52\rangle$ (Ni1 $\uparrow$ ) $\rightarrow$ $ 50\rangle$ (Ni1 $\downarrow$ )                     | 99.5         | 0.001                                      | 1.655                   | 0.0049           | 371.0     | 280.0          | 120.7        | 26.8           |
| $\Lambda 19$      | $ 50\rangle$ (Ni1 $\downarrow$ ) $\rightarrow$ $ 38\rangle$ (nonacene $\downarrow$ )              | 95.3         | 1.325                                      | 1.192                   | 0.0073           | 493.4     | 86.8           | -79.0        | 322.7          |
| $\Lambda 20$      | $ 1\rangle$ (Ni1 $\downarrow$ ) $\rightarrow$ $ 9\rangle$ (Ni1 $\downarrow$ )                     | 100.0        | 0.150                                      | 0.152                   | 0.0074           | 410.9     | 344.5          | 123.1        | 173.1          |
| $\Lambda 21$      | $ 17\rangle$ (Ni1 $\downarrow$ ) $\rightarrow$ $ 22\rangle$ (Ni1 and nonacene $\downarrow$ )      | 98.3         | 0.222                                      | 1.216                   | 0.0075           | 329.4     | 340.7          | 336.6        | 259.5          |
| $\Lambda 22$      | $ 18\rangle$ (Ni1 $\uparrow$ ) $\rightarrow$ $ 24\rangle$ (Ni1 and nonacene $\uparrow$ )          | 97.9         | 0.222                                      | 2.151                   | 0.0084           | 432.2     | 327.3          | 113.9        | 327.1          |
| $\Lambda 23$      | $ 49\rangle$ (nonacene $\uparrow$ ) $\rightarrow$ $ 24\rangle$ (Ni1 and nonacene $\uparrow$ )     | 100.0        | 1.626                                      | 1.629                   | 0.0027           | 487.8     | 243.9          | 68.9         | 24.5           |
| $\Lambda 24$      | $ 49\rangle$ (nonacene $\uparrow$ ) $\rightarrow$ $ 47\rangle$ (nonacene $\downarrow$ )           | 88.5         | 0.001                                      | 0.427                   | 0.0049           | 379.7     | 103.2          | 17.3         | 84.9           |
| $\Lambda 25$      | $ 47\rangle$ (nonacene $\downarrow$ ) $\rightarrow$ $ 22\rangle$ (Ni1 and nonacene $\downarrow$ ) | 100.0        | 1.626                                      | 1.619                   | 0.0072           | 144.7     | 286.2          | 2.9          | 162.4          |

through the process  $\Lambda 21$  the systems goes to state  $|22\rangle$  (bit 0, since it's a spin-down state with spin doubly localized on Ni1 and nonacene) with a high fidelity of 98.3%. Combining with the scenarios  $\Lambda 22$ ,  $\Lambda 16$  and  $\Lambda 23$ , and  $\Lambda 24$  and  $\Lambda 25$ , the whole function of the XOR gate can be accomplished within around 3.365 ps.

The details of the laser pulses ( $\Lambda 15 \sim \Lambda 25$ ) for these two logic gates can be found in Table V. For the technical feasibility of the above proposed scheme, there are three main aspects that need to cooperate: (i) the detection of the defined bit information, (ii) the implementation of the specified laser pulses, and (iii) the preparation of the corresponding states (which proves to be theoretically possible previously either through the ERASE functionality [58] or an additional  $\Lambda$  process [64]). With the development of recent experimental techniques, we highly expect that these dynamics and functions will eventually be realized in the near future. Another concern is that when being used in a device, these predicted scenarios and gates would be totally destroyed by the interactions with substrate or leads and become undetectable. About this point, it has been reported that the predicted spin state of the boron-substituted graphene nanoribbons can be experimentally detected by lifting it to lie freestanding between the STM (i.e., scanning tunneling microscopy) tip and surface [65]. This suspending route can dissociate the strong interaction between the sample and metal substrate, and thus largely preserve the predicted effects and to some extent allay this concern. On the other hand, the TM-carbon systems of interest is towards the goal of all-carbon molecular spintronics (although preliminary and challenging), which has achieved extraordinary developments in recent years and a series of corresponding devices with carbon chain, carbon nanotubes,

graphene, and graphene nanoribbons as electrodes or substrate materials [66–68] have been constructed. In this respect, our present paper can be preliminarily considered to involve the interaction with leads (e.g., carbon chain [44] and  $n$ -acene molecule) or substrates (e.g., graphene flakes [47]) and make a necessary and essential attempt at further, more realistic devices.

## VII. SUMMARY

Using high-level quantum chemistry method we systematically investigate the electronic structure, spin localization, and laser-induced ultrafast spin dynamics in the Ni-( $C_{4n+2}H_{2n+2}$ )-Ni complexes ( $n = 4 \sim 9$ ). The results are summarized as follows:

(i) The optimized geometry of each structure proves to be stable and the distinguishability of the two Ni-C bonds can give rise to spin localization (and thus enables spin transfer possible). For the level distribution of the six structures with the same amount of lowest states, it's found that the states with spin localized on single magnetic atom mainly concentrate below 0.61 eV, the states with spin localized on linearly fused benzene rings are located in the higher energy region, and the region between between 0.74 and 1.35 eV only accommodates nonlocalized states. As the carbon chain becomes longer, the amount the states with spin singly localized on Ni atoms increases. For the anisotropy of the structures, we find the spin localized states when the magnetic field is applied perpendicularly to the molecular plane are less than those when the field direction is within the molecular plane.

(ii) Under appropriate laser pulses, different types of spin-transfer scenarios have been achieved in different structures.

TABLE VI. The information of the MOs (including HOMO and LUMO) of the structures and the main virtual excitations contributing to their SAC-CI ground states.

| Structures                                | Total number of MOs | HOMO and LUMO with energies              | Main virtual excitations for the ground states |
|---|---------------------|--|--|
| $\text{Ni}_2(\text{C}_{18}\text{H}_{10})$ | 148                 | MO 77 (−3.414 eV)<br>MO 78 (−1.012 eV)   | MO 65 → MO 91 0.879 MO 65 → MO 86 0.266        |
|   |                     |  | MO 65 → MO 106 −0.179 MO 65 → MO 98 0.131      |
|   |                     |  | MO 65 → MO 105 0.112 MO 65 → MO 144 −0.107     |
|   |                     |  | MO 77 → MO 91 and MO 65 → MO 86 −0.178         |
|   |                     |  | MO 77 → MO 86 and MO 65 → MO 91 −0.124         |
| $\text{Ni}_2(\text{C}_{22}\text{H}_{12})$ | 170                 | MO 90 (−3.722 eV)<br>MO 91 (−1.713 eV)   | MO 90 → MO 91 0.889 MO 90 → MO 92 0.214        |
|   |                     |  | MO 90 → MO 106 and MO 90 → MO 91 0.312         |
|   |                     |  | MO 85 → MO 106 and MO 90 → MO 91 0.167         |
|   |                     |  | MO 90 → MO 113 and MO 90 → MO 91 −0.160        |
|   |                     |  | MO 88 → MO 100 and MO 90 → MO 91 0.126         |
| $\text{Ni}_2(\text{C}_{26}\text{H}_{14})$ | 192                 | MO 103 (−3.515 eV)<br>MO 104 (−1.493 eV) | MO 92 → MO 119 0.877 MO 92 → MO 112 0.274      |
|   |                     |  | MO 92 → MO 140 −0.180 MO 92 → MO 139 −0.132    |
|   |                     |  | MO 92 → MO 127 0.128 MO 92 → MO 188 −0.105     |
|   |                     |  | MO 103 → MO 119 and MO 92 → MO 119 −0.262      |
|   |                     |  | MO 103 → MO 119 and MO 92 → MO 112 −0.191      |
| $\text{Ni}_2(\text{C}_{30}\text{H}_{16})$ | 214                 | MO 116 (−3.347 eV)<br>MO 117 (−1.279 eV) | MO 103 → MO 112 and MO 92 → MO 119 −0.131      |
|   |                     |  | MO 100 → MO 130 −0.823 MO 115 → MO 130 0.308   |
|   |                     |  | MO 100 → MO 124 −0.266 MO 100 → MO 151 0.203   |
|   |                     |  | MO 115 → MO 124 0.130 MO 100 → MO 140 −0.109   |
|   |                     |  | MO 115 → MO 130 and MO 100 → MO 130 0.242      |
| $\text{Ni}_2(\text{C}_{36}\text{H}_{18})$ | 236                 | MO 129 (−3.213 eV)<br>MO 130 (−1.071 eV) | MO 115 → MO 130 and MO 100 → MO 124 0.146      |
|   |                     |  | MO 115 → MO 124 and MO 100 → MO 130 0.115      |
|   |                     |  | MO 111 → MO 144 0.855 MO 111 → MO 137 0.302    |
|   |                     |  | MO 111 → MO 166 0.210 MO 128 → MO 144 −0.120   |
|   |                     |  | MO 111 → MO 154 −0.101 MO 111 → MO 231 −0.100  |
| $\text{Ni}_2(\text{C}_{38}\text{H}_{20})$ | 258                 | MO 142 (−3.102 eV)<br>MO 143 (−1.889 eV) | MO 128 → MO 144 and MO 111 → MO 144 0.277      |
|   |                     |  | MO 128 → MO 144 and MO 111 → MO 137 0.233      |
|   |                     |  | MO 128 → MO 137 and MO 111 → MO 144 0.164      |
|   |                     |  | MO 123 → MO 158 0.877 MO 123 → MO 150 0.277    |
|   |                     |  | MO 123 → MO 181 −0.222 MO 123 → MO 169 0.123   |
|   |                     |  | MO 123 → MO 253 −0.109                         |
|   |                     |  | MO 141 → MO 158 and MO 123 → MO 158 0.232      |
|   |                     |  | MO 141 → MO 158 and MO 123 → MO 150 −0.147     |
|   |                     |  | MO 141 → MO 150 and MO 123 → MO 158 −0.112     |

Specifically, spin transfer between state with spin localization on Ni1 and state with spin localization on Ni2 is only achieved in structures  $\text{Ni}_2(\text{C}_{18}\text{H}_{10})$ ,  $\text{Ni}_2(\text{C}_{22}\text{H}_{12})$  and  $\text{Ni}_2(\text{C}_{38}\text{H}_{20})$ , spin transfer between state with spin localized on Ni1/Ni2 and state with spin localized on  $\text{C}_{4n+2}\text{H}_{2n+2}$  is only found in  $\text{Ni}_2(\text{C}_{22}\text{H}_{12})$ ,  $\text{Ni}_2(\text{C}_{26}\text{H}_{14})$  and  $\text{Ni}_2(\text{C}_{38}\text{H}_{20})$ . Although there exist several states with different spin localization on Ni1 and Ni2 for structures  $\text{Ni}_2(\text{C}_{30}\text{H}_{16})$  and  $\text{Ni}_2(\text{C}_{34}\text{H}_{18})$ , the transfer between them through one single  $\Lambda$  process is not achievable. The reason can be attributed to (a) the absence of the common intermediate states that have both transitions with the selected initial and final states, (b) the unbalanced transition strengths of the two branches of the  $\Lambda$  process, or (c) strong level interspersing of the adjacent localized candidate initial and final states. In addition, it's found that the transfer between states with different spin localizations on Ni1 and Ni2 through the

combination of several spin-merge and -bifurcation processes can be realized, which provides additional channels for the realization of certain spin functions.

(iii) Based on the achieved spin scenarios, by choosing the spin scenarios and designing the bit according to the spin localization and spin directions of the states, two types of logic gates, i.e., SWAP and XOR, for structure  $\text{Ni}_2(\text{C}_{38}\text{H}_{20})$  are constructed, which both complete within picosecond time scales with high fidelity above 88.0%.

All these theoretical predictions are expected to provide valuable information for the experimental probe and realization of ultrafast laser-driven magnetization in linearly fused Ni substituted polyacenes complexes, and promote the application towards the ultrafast, high-density molecular spintronic devices and future spin-based quantum computing.

## ACKNOWLEDGMENTS

We acknowledge financial support from the National Natural Science Foundation of China (Grants No. 11504223, No. 11872309, and No. 11572251) the Natural Science Basic Research Program of Shaanxi Province (Grant No. 2022JC-02), and the Guangdong Basic and Applied Basic Research Foundation (Grant No. 2022A1515010633).

## APPENDIX

Table VI gives the information of the molecular orbitals (MOs, including HOMO and LUMO) of the structures and the main single and double virtual excitations (with coefficients above 0.100) that contribute to their ground states. We see that the total number of MOs increases with the size the structures,

however the HOMO-LOMO gap values (around 2 eV) of them are quite close. For the electronic states obtained from the SAC-CI method, since each one is constructed by the linear combination of various determinants based on virtual excitations between different MOs, going to larger basis set will give rise to the increase of the Fock space and thus numerous virtual excitations that make the calculation complex and costly (without bringing any new physics). Thus the moderate combined basis (i.e., Lan12dz for magnetic atoms and STO-3G for the rest light atoms) is chosen based on the compromise between the calculation cost and accuracy. In addition, from the virtual excitations we see that the dominant determinant (the one with the largest coefficient) for each ground state comes from single excitation. The double excitations, although with smaller coefficients, are also important since they can become dominant with the large amount of related determinant terms.

- 
- [1] E. C. Ahn, *npj 2D Mater. Appl.* **4**, 17 (2020).
- [2] Z. C. Lawrence, H. K. Isaac, D. B. Stephen, and J. B. Benjamin, *Sci. Adv.* **8**, eabn1717 (2022).
- [3] E. Beaupaire, J.-C. Merle, A. Daunois, and J.-Y. Bigot, *Phys. Rev. Lett.* **76**, 4250 (1996).
- [4] B. Koopmans, J. J. M. Ruijgrok, F. Dalla Longa, and W. J. M. de Jonge, *Phys. Rev. Lett.* **95**, 267207 (2005).
- [5] G. P. Zhang, W. Hübner, G. Lefkidis, Y. Bai, and T. F. George, *Nat. Phys.* **5**, 499 (2009).
- [6] M. Battiato, K. Carva, and P. M. Oppeneer, *Phys. Rev. Lett.* **105**, 027203 (2010).
- [7] S. Mangin, M. Gottwald, C.-H. Lambert, D. Steil, V. Uhlř, L. Pang, M. Hehn, S. Alebrand, M. Cinchetti, G. Malinowski, Y. Fainman, M. Aeschlimann, and E. E. Fullerton, *Nat. Mater.* **13**, 286 (2014).
- [8] A. Stupakiewicz, K. Szerenos, D. Afanasiev, A. Kirilyuk, and A. V. Kimel, *Nature (London)* **542**, 71 (2017).
- [9] A. Hirohata, K. Yamada, Y. Nakatani, I.-L. Prejbeanu, B. Diény, P. Pirro, and B. Hillebrands, *J. Magn. Magn. Mater.* **509**, 166711 (2020).
- [10] X. Xue, M. Russ, N. Samkharadze, B. Undseth, A. Sammak, G. Scappucci, and L. M. K. Vandersypen, *Nature (London)* **601**, 343 (2022).
- [11] J.-I. Aihara and H. Kanno, *J. Phys. Chem. A* **109**, 3717 (2005).
- [12] P. Bultinck, R. Ponc, and R. Carbó-Dorca, *J. Comput. Chem.* **28**, 152 (2007).
- [13] H. Chakraborty and A. Shukla, *J. Phys. Chem. A* **117**, 14220 (2013).
- [14] Q. Ye and C. Y. Chi, *Chem. Mater.* **26**, 4046 (2014).
- [15] T. Enoki and M. Kiguchi, *Phys. Rev. Appl.* **9**, 037001 (2018).
- [16] C. Zeiser, C. Cruz, D. R. Reichman, M. Seitz, J. Hagenlocher, E. L. Chronister, C. J. Bardeen, R. Tempelaar, and K. Broch, *Nat. Commun.* **12**, 5149 (2021).
- [17] J. Medina Dueñas, H. L. Calvo, and L. E. F. Foa Torres, *Phys. Rev. Lett.* **128**, 066801 (2022).
- [18] A. Kuc, T. Heine, and G. Seifert, *Phys. Rev. B* **81**, 085430 (2010).
- [19] X. Wang, J. Z. Sun, and B. Z. Tang, *Prog. Polym. Sci.* **79**, 98 (2018).
- [20] B. S. Hudson, *Materials* **11**, 242 (2018).
- [21] G. Prunet, F. Pawula, G. Fleury, E. Cloutet, A. Robinson, G. Hadziioannou, and A. Pakdel, *Mater. Today Phys.* **18**, 100402 (2021).
- [22] H. F. Bettinger and C. Tönshoff, *Chem. Rec.* **15**, 364 (2015).
- [23] T. Kitao, T. Miura, R. Nakayama, Y. Tsutsui, Y. S. Chan, H. Hayashi, H. Yamada, S. Seki, T. Hitosugi, and T. Uemura, *Nat. Synth.* **2**, 848 (2023).
- [24] J. Zhu, C. Dahlstrand, J. R. Smith, S. Villaume, and H. Ottosson, *Symmetry* **2**, 1653 (2010).
- [25] M. M. Payne, S. R. Parkin, and J. E. Anthony, *J. Am. Chem. Soc.* **127**, 8028 (2005).
- [26] J. E. Anthony, *Chem. Rev.* **106**, 5028 (2006).
- [27] J. S. Wu, W. Pisula, and K. Müllen, *Chem. Rev.* **107**, 718 (2007).
- [28] D. Chun, Y. Cheng, and F. Wudl, *Angew. Chem. Int. Ed.* **47**, 8380 (2008).
- [29] B. Hajgató, D. Szieberth, P. Geerlings, F. De. Proft, and M. S. Deleuze, *J. Chem. Phys.* **131**, 224321 (2009).
- [30] C. Tönshoff and H. F. Bettinger, *Angew. Chem. Int. Ed.* **49**, 4125 (2010).
- [31] J. Krüger, F. García, F. Eisenhut, D. Skidin, J. M. Alonso, E. Guitián, D. Pérez, G. Cuniberti, F. Moresco, and D. Peña, *Angew. Chem. Int. Ed.* **56**, 11945 (2017).
- [32] A. Jančařfk, J. Holec, Y. Nagata, M. Šámal, and A. Gourdon, *Nat. Commun.* **13**, 223 (2022).
- [33] K. Eimre, J. I. Urgel, H. Hayashi, M. D. Giovannantonio, P. Ruffieux, S. Sato, S. Otomo, Y. S. Chan, N. Aratani, D. Passerone, O. Gröning, H. Yamada, R. Fasel, and C. A. Pignedoli, *Nat. Commun.* **13**, 511 (2022).
- [34] P. M. Beaujuge and J. M. J. Fréchet, *J. Am. Chem. Soc.* **133**, 20009 (2011).
- [35] J. Hwang, C. D. Sunesh, M. Chandran, J. Lee, and Y. Choe, *Org. Electron.* **13**, 1809 (2012).
- [36] Y. Yang, E. R. Davidson, and W. T. Yang, *Proc. Natl. Acad. Sci. USA* **113**, E5098 (2016).
- [37] W. D. Zeng and J. S. Wu, *Chem* **7**, 358 (2021).
- [38] D.-E. Jiang and S. Dai, *J. Phys. Chem. A* **112**, 332 (2008).
- [39] M. Bendikov, H. M. Duong, K. Starkey, K. N. Houk, E. A. Carter, and F. Wudl, *J. Am. Chem. Soc.* **126**, 7416 (2004).

- [40] Y. Y. Miao, L. Y. Chen, G. P. Zhang, C. K. Wang, J. F. Ren, C. Timm, and G. C. Hu, *Phys. Rev. B* **105**, 094419 (2022).
- [41] İ. Muz, F. Göktaş, and M. Kurban, *Theor. Chem. Acc.* **139**, 23 (2020).
- [42] C.-H. Lambert, S. Mangin, B. S. D. C. S. Varaprasad, Y. K. Takahashi, M. Hehn, M. Cinchetti, G. Malinowski, K. Hono, Y. Fainman, M. Aeschlimann, and E. E. Fullerton, *Science* **345**, 1337 (2014).
- [43] R. Pilevarshahri, I. Rungger, T. Archer, S. Sanvito, and N. Shahtahmassebi, *Phys. Rev. B* **84**, 174437 (2011).
- [44] J. Liu, C. Li, W. Jin, G. Lefkidis, and W. Hübner, *Phys. Rev. Lett.* **126**, 037402 (2021).
- [45] J. Liu, Y. M. Zhang, C. Li, W. Jin, G. Lefkidis, and W. Hübner, *Phys. Rev. B* **106**, 094401 (2022).
- [46] Y.-M. Zhang, J. Liu, C. Li, W. Jin, G. Lefkidis, and W. Hübner, *Appl. Surf. Sci.* **558**, 149770 (2021).
- [47] Y.-M. Zhang, J. Liu, W. Jin, G. Lefkidis, W. Hübner, and C. Li, *Carbon* **193**, 195 (2022).
- [48] M. J. Frisch, G. W. Trucks, H. B. Schlegel, G. E. Scuseria, M. A. Robb, J. R. Cheeseman, G. Scalmani, V. Barone, G. A. Petersson, H. Nakatsuji, X. Li, M. Caricato, A. V. Marenich, J. Bloino, B. G. Janesko, R. Gomperts, B. Mennucci, H. P. Hratchian, J. V. Ortiz, A. F. Izmaylov *et al.*, *Gaussian16 Revision B.01* (Gaussian Inc., Wallingford, CT, 2016).
- [49] P. J. Hay and W. R. Wadt, *J. Chem. Phys.* **82**, 299 (1985).
- [50] H. Nakatsuji, *Chem. Phys. Lett.* **67**, 329 (1979).
- [51] W. Jin, F. Rupp, K. Chevalier, M. M. N. Wolf, M. C. Rojas, G. Lefkidis, H.-J. Krüger, R. Diller, and W. Hübner, *Phys. Rev. Lett.* **109**, 267209 (2012).
- [52] X.-F. Liang, J.-Y. Yang, Y.-M. Zhang, J. Liu, C. Li, G. Lefkidis, W. Hübner, and W. Jin, *Phys. Chem. Chem. Phys.* **24**, 24881 (2022).
- [53] C. Li, J. Liu, S.-B. Zhang, G. Lefkidis, and W. Hübner, *Carbon* **87**, 153 (2015).
- [54] S. Koseki, M. W. Schmidt, and M. S. Gordon, *J. Phys. Chem. A* **102**, 10430 (1998).
- [55] R. Gómez-Abal, O. Ney, K. Satitkovitchai, and W. Hübner, *Phys. Rev. Lett.* **92**, 227402 (2004).
- [56] J. R. Cash and A. H. Karp, *ACM Trans. Math. Softw.* **16**, 201 (1990).
- [57] T. Hartenstein, C. Li, G. Lefkidis, and W. Hübner, *J. Phys. D* **41**, 164006 (2008).
- [58] C. Li, S.-B. Zhang, W. Jin, G. Lefkidis, and W. Hübner, *Phys. Rev. B* **89**, 184404 (2014).
- [59] W. Jin, C. Li, G. Lefkidis, and W. Hübner, *Phys. Rev. B* **89**, 024419 (2014).
- [60] D. Chaudhuri, G. Lefkidis, and W. Hübner, *Phys. Rev. B* **96**, 184413 (2017).
- [61] N. Zhang, H. Du, J. Chang, W. Jin, C. Li, G. Lefkidis, and W. Hübner, *Phys. Rev. B* **98**, 104431 (2018).
- [62] M.-L. Xie, Y.-T. Zheng, J. Liu, W. Jin, C. Li, G. Lefkidis, and W. Hübner, *Phys. Rev. B* **103**, 054433 (2021).
- [63] B. C. Mummaneni, J. Liu, G. Lefkidis, and W. Hübner, *J. Phys. Chem. Lett.* **13**, 2479 (2022).
- [64] G. Lefkidis, W. Jin, J. Liu, D. Dutta, and W. Hübner, *J. Phys. Chem. Lett.* **11**, 2592 (2020).
- [65] N. Friedrich, P. Brandimarte, J. C. Li, S. H. Saito, S. Yamaguchi, I. Pozo, D. Peña, T. Frederiksen, A. Garcia-Lekue, D. Sánchez-Portal, and J. I. Pascual, *Phys. Rev. Lett.* **125**, 146801 (2020).
- [66] E. Lörtscher, *Nat. Nanotechnol.* **8**, 381 (2013).
- [67] Y.-X. Lin, Y. Cao, S.-J. Ding, P.-P. Zhang, L. Xu, C.-C. Liu, Q.-L. Hu, C.-H. Jin, L.-M. Peng, and Z.-Y. Zhang, *Nat. Electron.* **6**, 506 (2023).
- [68] W.-F. Zhang, G.-P. Zhang, Z.-L. Li, X.-X. Fu, C.-K. Wang, and M.-L. Wang, *Phys. Chem. Chem. Phys.* **24**, 1849 (2022).